Large Eddy Simulations of Electromagnetic Braking Effects on Argon Bubble Transport and Capture in a Steel Continuous Casting Mold

KAI JIN, SURYA P. VANKA, and BRIAN G. THOMAS

In continuous casting of steel, argon gas is often injected to prevent clogging of the nozzle, but the bubbles affect the flow pattern, and may become entrapped to form defects in the final product. Further, an electromagnetic field is frequently applied to induce a braking effect on the flow field and modify the inclusion transport. In this study, a previously validated GPU-based in-house code CUFLOW is used to investigate the effect of electromagnetic braking on turbulent flow, bubble transport, and capture. Well-resolved large eddy simulations are combined with two-way coupled Lagrangian computations of the bubbles. The drag coefficient on the bubbles is modified to account for the effects of the magnetic field. The distribution of the argon bubbles, capture, and escape rates, are presented and compared with and without the magnetic field. The bubble capture patterns are also compared with results of a previous RANS model as well as with plant measurements.

https://doi.org/10.1007/s11663-018-1191-1

I. INTRODUCTION

In continuous casting of steel, argon gas is often injected to prevent clogging of the nozzle.[1–3] However, the gas injection also modifies the flow pattern due to two-way coupling between the bubbles and the turbulent flow field. After entering the Submerged Entry Nozzle (SEN), argon bubbles are carried by the turbulent flow into the mold cavity region, where they affect the flow pattern, surface level fluctuations, and slag entrainment. Larger bubbles entering the mold region may either end up at the top surface and escape harmlessly into the atmosphere,[4,5] or get captured near the meniscus and lead to surface defects, while smaller bubbles may reside deep in the caster and cause internal defects. In addition, during their transport, the bubbles collect nonwetting inclusion particles such as alumina and can cause severe sliver defects.[6,7]

Computational and water models have been previously[4–23] used to understand the flow of argon gas and molten steel in the SEN and mold regions of the continuous caster. The computational models used both Eulerian–Lagrangian[5,8–14,16,24] and Eulerian–Eulerian[9,17–19,25] approaches including two-way coupling at high gas fractions.[8–10,20] Increasing Ar gas causes increased upward flow near the SEN and tends to alter the classic double-roll flow pattern to a single-roll with surface flows away from the SEN and toward the narrow face.[9,18,19] Excessive gas fractions have also been observed to lead to oscillating and asymmetric flow.[1,26] Traditional Eulerian–Eulerian models have been recently combined with the MUltiple SIze Group (MUSIG) model[27] to include the effect of multiple local bubble sizes.[20,28]

Several previous studies[10,12–16,21,23,29–31] have also investigated the capture of inclusion particles, but none of these studies included the effects of Ar gas on the flow field. Recently,[4,5] the Reynolds-Averaged Navier Stokes (RANS) approach was applied with a Lagrangian approach to study the transport and capture of argon bubbles. The turbulent dispersion of individual bubbles was represented by a random walk method[10,11,14–16,20–24,29,30] and included the effects of bubbles of different diameter on the local fluid flow. Using an advanced capture criterion,[13,14,22] it was found that only a small fraction of large bubbles is captured (< 0.02 pct), but ~ 85 pct of small (< 0.08 mm) bubbles are captured. The predicted capture location and size of bubbles matched with plant experiments in most places except in a region close to the meniscus.

The velocity across the top surface region of the mold is an important parameter affecting defect formation. Electromagnetic braking (EMBr) with local,[11,32–36]

KAI JIN and SURYA P. VANKA are with the Department of Mechanical Science and Engineering, University of Illinois at Urbana Champaign, Urbana, IL 61801. BRIAN G. THOMAS is with the Department of Mechanical Science and Engineering, University of Illinois at Urbana Champaign and also with the Department of Mechanical Engineering, Colorado School of Mines, Golden, CO 80401. Contact e-mail: bgthomas@illinois.edu

Manuscript submitted March 13, 2017.
Article published online February 20, 2018.

single-ruler,[36–41] and double-ruler[18,41–46] configurations have been studied. In the widely used double-ruler configuration (known as the FC-Mold), two rectangular magnetic fields across the mold width are generated, with one positioned near the meniscus and the other below the nozzle ports.[18,42–45,47] This configuration is able to slow down[42,45,46] as well as speed up[41,44] surface velocities in the mold region, decrease high-frequency turbulent fluctuations,[41] and thereby improve meniscus stability.[44–46]

The RANS approach with Lagrangian particle tracking has been previously used to study the effect of argon bubbles on inclusion capture including the effects of the EMBr.[11,18,48] These studies showed that the EMBr has little effect on the removal fraction of small bubbles,[11,18] but ignored the effects of a conducting shell, which is observed to stabilize the flow and suppress the unsteady low-frequency oscillatory behavior of the flow.[40,41] The RANS approach does not resolve the time-dependent transport of the bubbles and instead models it through a statistical approach.

In this study, we investigate the transport and capture of argon bubbles using a LES model for the turbulent flow and Lagrangian description for argon bubbles, including the effects of the magnetic field on the large scales of turbulence. We also include the solidified shell and the effect of EMBr on bubble drag force through a modified drag coefficient.[49] The LES results are compared with previous RANS simulations and plant measurements.[4,5]

II. COMPUTATIONAL MODEL

In this study, a three-dimensional finite-volume computational model together with two-way coupled Lagrangian particle tracking is applied to study the fully coupled turbulent flow behavior and the transport of argon bubbles in a commercial continuous steel caster. The computational domain includes the slide gate, SEN and straight mold region (from meniscus surface to 2.65 m below meniscus, which is above the bending region), as shown in Figure 1.[50] In the plant operation, 1300 mm wide slabs were cast at 1.5 m/min, and the slide gate was 70 pct open,[4,5] as shown in Figure 2(a).[50] The computational domain was discretized into ~ 16 million hexahedral finite-volume ~cubic cells with edge length ~ 4 mm. Casting conditions are taken as described in references[4,5] and listed in Table I. The assumed shell thickness s (mm) at any point z (m) below the top surface is calculated as

$$s = k\sqrt{z/V_c}, \qquad [1]$$

where $V_c = 0.025$ m/s (1.5 m/min) denotes the casting speed, and the constant $k = 3$ mm/s$^{1/2}$ is chosen to match the break-out shell profile from the caster at Baosteel company in China. This caster also has a double-ruler electromagnetic braking system (EMBr) installed. Figure 2(b) shows the measured magnetic field strength $(B_x, B_y, B_z) = (0, B, 0)$ (dots, provided by Baosteel and ABB), and the fitted line is used in the simulation. Although the field B_y is plotted with its sign, only its magnitude affects the flow, and thus the field effect is minimal across the ports.

A. *Governing Equations for the Fluid Flow*

In this work the turbulent flow in the SEN and the mold is simulated by the LES approach. The following three-dimensional time-dependent Navier Stokes equations were solved:

$$\nabla \cdot (\rho \boldsymbol{u}) = \dot{s} \qquad [2]$$

$$\rho\frac{\partial \boldsymbol{u}}{\partial t} + \rho(\boldsymbol{u}\cdot\nabla)\boldsymbol{u} = -\nabla p + \nabla\cdot\left[(\mu+\mu_{sgs})\left(\nabla\boldsymbol{u}+\nabla\boldsymbol{u}^T\right)\right] + \boldsymbol{S}_L + \boldsymbol{S}_{sink} + \boldsymbol{S}_p \qquad [3]$$

where ρ is the density of molten steel, $\dot{s}$ and $\boldsymbol{S}_{sink}$ are the mass and momentum sink terms[5,13,46,51] added to include the effects of the solidifying shell, $\boldsymbol{u}$ is the velocity vector, p is a modified static pressure which includes the normal stresses, $\boldsymbol{S}_p$ are the source terms due to two-way coupled Lagrangian particle tracking, μ is the dynamic viscosity of the molten steel, and μ_{sgs} is the eddy viscosity that represents the subgrid stress. The imposed magnetic field affects the fluid flow through the Lorentz force field source term $\boldsymbol{S}_L$, as discussed below. In this study, top-hat filtering is applied across the cell width *via* the finite-volume discretization; μ_{sgs} is modeled by the coherent-structure Smagorinsky model (CSM) of subgrid scales (SGS).[52] In the CSM SGS model, μ_{sgs} is computed as:

$$\mu_{sgs} = \rho\nu_{sgs} = \rho(C_s\Delta)^2\sqrt{2\|\mathbf{S}\|^2} \qquad [4]$$

where $\Delta = V_{cell}^{(1/3)}$ is the filter width, V_{cell} is the volume of the cell, and $\mathbf{S}$ is the rate-of-strain tensor given by $\mathbf{S} = \frac{1}{2}(\nabla\boldsymbol{u} + \nabla\boldsymbol{u}^T)$. C_s^2 is calculated locally by the following equations:

$$C_s^2 = C_{CSM}\left|\frac{Q}{E}\right|^{3/2}\left(1-\frac{Q}{E}\right) \qquad [5]$$

$$Q = \frac{1}{2}\left(\|\mathbf{W}\|^2 - \|\mathbf{S}\|^2\right) \quad E = \frac{1}{2}\left(\|\mathbf{W}\|^2 + \|\mathbf{S}\|^2\right), \qquad [6]$$

where $C_{CSM} = 1/22$ is a model constant, $\mathbf{W} = \frac{1}{2}(\nabla\boldsymbol{u} - \nabla\boldsymbol{u}^T)$ is the vorticity tensor, Q is the 2nd invariant, and E is the magnitude of the velocity gradient tensor. The eddy viscosity is modeled by a coherent-structure function (CSF) with a model constant (C_{CSM}).[52] The CSM model appropriately damps the eddy viscosity in wall boundary layer regions and also automatically incorporates the effect of anisotropy induced by the applied magnetic fields on the subgrid scales.[53] Therefore, no additional modifications to account for anisotropic subgrid effects are needed.

This model has been successfully tested previously in predicting single phase fluid flow in steel casters with magnetic fields.[40,44,46] The flow at the inlet is assumed to have constant velocity to match the volumetric flow rate of 0.4485 m^3/min. Since the bottom of the computational domain is far from the mold region, flow leaving the bottom is assumed to have a constant speed of 1.5 m/min. Moving wall boundary conditions ($v_z = V_c$) are applied at interfaces between liquid steel and solidified shell. No slip and no penetration boundary conditions are applied at all other boundaries. This includes the top surface, where previous study has shown that the high-viscosity slag layer acts almost like a solid wall, slowing transverse movement of the slag–steel interface to just a few mm/s.[54]

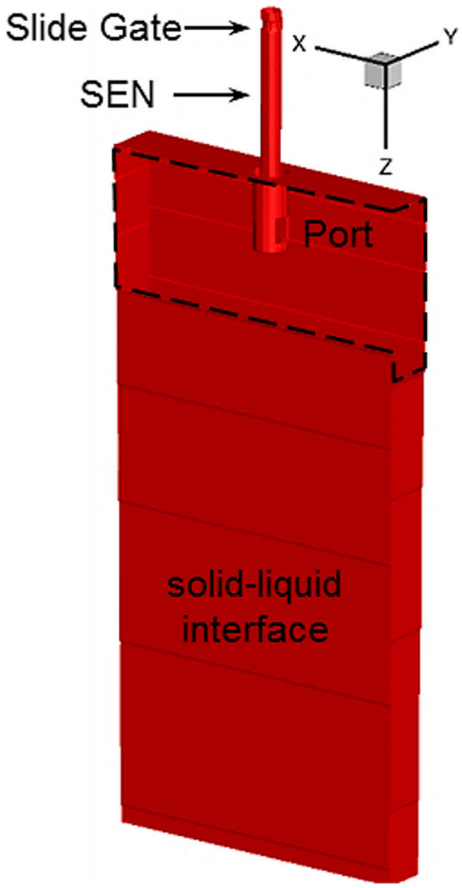

Fig. 1—Computational domain including slide gate, SEN, and mold region down to 2.7 m beneath the top surface. Reprinted with permission from Ref. [50].

The Lorentz force source term $\boldsymbol{S}_L$ is calculated using the electric potential method, which exploits the fact that the induced magnetic field is much smaller than the externally imposed magnetic field.[18,34,35,37–42,44,55] The Lorentz force per unit volume is calculated by first solving a Poisson equation for the electric potential Φ and then computing the current density $\boldsymbol{J}$.[46,49]

$$\nabla \cdot (\sigma \nabla \Phi) = \nabla \cdot [\sigma(\mathbf{u} \times \mathbf{B})] \quad [7]$$

$$\boldsymbol{J} = \sigma(-\nabla \Phi + \mathbf{u} \times \mathbf{B}) \quad [8]$$

$$\boldsymbol{S}_L = (\mathbf{J} \times \mathbf{B}) \quad [9]$$

Note that both the molten steel and the solidified shell are conducting materials, so the equations related to the current must be solved in both the liquid steel and shell regions. Replacing the shell with an electrically insulated wall boundary condition leads to incorrect results, as discussed elsewhere.[40,41] Thus, in this study, the above MHD equations are solved in the entire domain including the solid shell region. An insulated condition is applied at the exterior of the shell, considering that the slag in the mold/shell gap has very low conductivity.

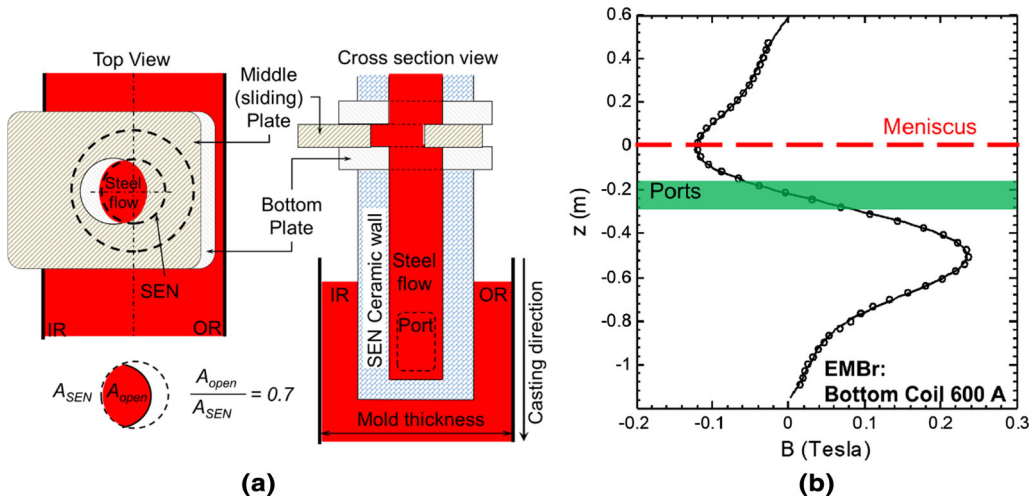

Fig. 2—(*a*) Schematic of slide gate opening and slide gate position. Reprinted with permission from Ref. [50]. (*b*) Measured (dots) and applied (line) magnetic field.

Table I. Process Parameters

Process Parameters	Value
Mold thickness (L_t)	230 mm
Mold width (L_w)	1300 mm
SEN submergence depth	160 mm
Nozzle port downward angle	15 deg
Nozzle port area (width × height)	65 × 83 mm^2
Casting speed (V_c)	1.5 m/min
Argon injection rate	9.2 SLPM (1 atm, 273 K) (cold) 40.1 LPM (1.4 atm, 1827K) (hot)
Argon volume fraction (α)	8.2 vol pct (hot)
Steel density (ρ)	7000 kg/m^3
Argon density (ρ_p)	0.5 kg/m^3
Steel viscosity (μ)	0.0063 kg/(m s)
Argon viscosity (μ_p)	0.0000212 kg/(m s)

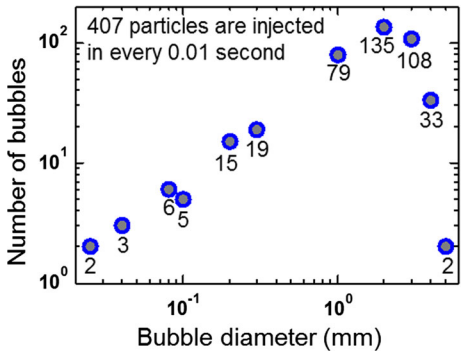

Fig. 3—Size distribution of injected bubbles. Reprinted with permission from Ref. [50].

B. *Lagrangian Model for Argon Bubbles*

In plant operation, argon gas is injected to prevent clogging. In this model, the total Ar gas volume injected through the porous refractory in the upper tundish nozzle and SEN was distributed into bubbles according to a Rosin–Rammler[56] distribution with an average bubble diameter d_{mean} of 3 mm and spread parameter η of 4, as in previous RANS simulations.[4,5] These parameters were based on a validated two-stage model of argon injection into downward-flowing steel[1,57] with adjustments to account for increased surface tension in steel/argon using a relation from measurements[1,57,58] of bubble distributions. In the current study, 407 bubbles with this distribution are randomly placed in a 4-cm-high cylindrical region below the slide gate every 0.01 second, based on the hot-gas flow rate in Table I. The number distribution of bubbles is shown in Figure 3.[50] For a 30-second LES simulation, the trajectories of ~ 1.2 million bubbles are tracked by solving the following equations of motion for each individual argon bubble:

$$\frac{\mathrm{d}\boldsymbol{x}_\mathrm{p}}{\mathrm{d}t} = \boldsymbol{u}_\mathrm{p} \qquad [10]$$

$$m_\mathrm{p}\frac{\mathrm{d}\boldsymbol{u}_\mathrm{p}}{\mathrm{d}t} = \boldsymbol{F}_\mathrm{pT} = \sum\left(\boldsymbol{F}_\mathrm{pD} + \boldsymbol{F}_\mathrm{pL} + \boldsymbol{F}_\mathrm{pP} + \boldsymbol{F}_\mathrm{pA} + \boldsymbol{F}_\mathrm{pB}\right), \qquad [11]$$

where $\boldsymbol{u}_\mathrm{p}$ and $\boldsymbol{x}_\mathrm{p}$ are the particle velocity and location vectors, respectively. The total force, $\boldsymbol{F}_\mathrm{pT}$, acting on an individual bubble is the sum of five forces: drag force $\boldsymbol{F}_\mathrm{pD}$, lift force $\boldsymbol{F}_\mathrm{pL}$, added mass force $\boldsymbol{F}_\mathrm{pA}$, pressure gradient force $\boldsymbol{F}_\mathrm{pP}$, and buoyancy/gravity force $\boldsymbol{F}_\mathrm{pB}$. Note that the equations for the bubble motion are independent for each bubble and therefore can be solved in parallel. The response time of the particle is given by

$$\tau_\mathrm{p} = \frac{\rho_\mathrm{p} d_\mathrm{p}^2}{18\mu_\mathrm{f}} \qquad [12]$$

A smaller response time means the dispersed phase needs a very short time to respond to a change in velocity. The response time for a 1 mm bubble in liquid steel is ~10^{-6} s. Thus, the argon bubbles accelerate to respond to the motion of the liquid steel very quickly.

The drag force acting on a single bubble is calculated as

$$\boldsymbol{F}_\mathrm{pD} = \frac{C_\mathrm{D}}{24}\frac{18\mu}{d_\mathrm{p}^2}V_\mathrm{p}\left(\boldsymbol{u}_\mathrm{Fp} - \boldsymbol{u}_\mathrm{p}\right)Re_\mathrm{p}, \qquad [13]$$

where V_p is particle volume, Re_p is particle Reynolds number, $\boldsymbol{u}_\mathrm{Fp}$ is the fluid velocity at the particle location, and C_D is the drag coefficient. As argon bubbles deform during the motion in the turbulent flow, the drag coefficient is computed based on bubble Reynolds and Weber numbers as follows[59]:

$$C_\mathrm{D}\begin{cases} 16Re_\mathrm{p}^{-1} & Re_\mathrm{p} \le 0.49 \\ 20.68Re_\mathrm{p}^{-0.643} & 0.49 < Re_\mathrm{p} \le 100 \\ 6.3Re_\mathrm{p}^{-0.385} & 100 < Re_\mathrm{p} \\ We/3 & 100 < Re_\mathrm{p} \text{ and } Re_\mathrm{p} > 2065.1We^{-2.6} \\ 8/3 & 100 < Re_\mathrm{p} \text{ and } We > 8, \end{cases} \qquad [14]$$

where $We = \frac{\rho_l d\left|\boldsymbol{u}-\boldsymbol{u}_\mathrm{p}\right|^2}{\gamma_\mathrm{lg}}$ and γ_lg = 1.2 N/m is the surface tension between argon and steel. This model implicitly accounts for the bubble shape using the Weber number and was seen to predict the terminal rise velocities reasonably well. The drag law used in this study depends on We, which differs from what we used previously.[4,5] The difference is more important for large bubbles, because small bubbles with smaller Eötvös number stay spherical. The effect is small because over 90 pct of the bubbles in this study are ≤ 3 mm. Even for larger bubbles, bubble deformation is limited, due to the high surface tension between argon and liquid steel, which leads to only small differences in results, so the RANS and LES model results can still be compared.

In this study, when the magnetic field is applied, the drag coefficient is modified based on a recent computational study[49] by the authors, as

$$C_{D-MHD} = \begin{cases} C_D(1.0 + 1.5N + 7.06N^2) & \text{if} \quad 0 \le N < 0.245 \\ 1.8C_D & \text{if} \quad 0.245 \le \text{N} < 0.65 \end{cases}, \quad [15]$$

where $N = Ha^2/Re_p$ is the Stuart number, and Ha is the Hartmann number:

$$Ha = Bd_p\sqrt{(\sigma/\mu)} \quad [16]$$

Table II shows the effects of different magnetic strengths on reduction of bubble rise velocity. The larger bubbles are much more sensitive to the magnetic field, with a reduction in rise velocity around 7.4 pct for 4 mm diameter bubbles.

The lift force, pressure gradient force, added mass force, and buoyancy force are computed as follows:

$$\boldsymbol{F}_{pL} = C_L\rho V_p(\boldsymbol{u}_p - \boldsymbol{u}_{Fp}) \times (\nabla \times \boldsymbol{u}_{Fp}) \quad [17]$$

$$\boldsymbol{F}_{pP} = \rho V_p \frac{D\boldsymbol{u}_{Fp}}{Dt} \quad [18]$$

$$\boldsymbol{F}_{pA} = 0.5C_V\rho V_p\left(\frac{D\boldsymbol{u}_{Fp}}{Dt} - \frac{d\boldsymbol{u}_p}{dt}\right) \quad [19]$$

$$\boldsymbol{F}_{pB} = \boldsymbol{g}V_p(\rho_p - \rho), \quad [20]$$

where C_L and C_V are the lift and added mass coefficients, respectively. In this study, C_V is taken as 1.0,[60] and C_L is calculated using the Legendre and Magnaudet lift force model[61]:

$$C_L = \sqrt{\left(C_L^{lowRe}\right)^2 + \left(C_L^{highRe}\right)^2} \quad [21]$$

$$C_L^{highRe} = \frac{1}{2}\frac{1 + 16Re_p^{-1}}{1 + 29Re_p^{-1}} \text{ and } C_L^{lowRe} = 6\pi^{-2}(\text{Sr}Re_p)^{-0.5}J'(\varepsilon) \quad [22]$$

$$J'(\varepsilon) = J(\infty)\left(1 + 0.2\varepsilon^{-2}\right)^{-3/2} \text{ and } \varepsilon = \sqrt{\text{Sr}Re_p^{-1}}, \quad [23]$$

where $J(\infty) = 2.55$ is a constant and Sr is the shear rate of the fluid at the particle location.

The fluid velocity at each particle location is computed using a second order Lagrange polynomial interpolation[62,63] involving 27 surrounding fluid grid points. The dispersion of bubbles due to the subgrid motion is included by adding a subgrid velocity to the fluid velocity at the particle location. The subgrid kinetic energy k_{sgs} is computed in each finite-volume cell using the Yoshizawa SGS model[64] and the computed subgrid scale viscosity given as.

$$v_{sgs} = 0.066\Delta k_{sgs}^{1/2} \quad [24]$$

A random fluctuation velocity $\boldsymbol{\zeta u}_{sgs}$ is then added to the mean velocity $\boldsymbol{u}_{Fp}$ to compute the instantaneous velocity. $\boldsymbol{\zeta}$ is sampled from a standard normal distribution with mean of 0 and standard deviation of 1.0. At each time step (every ~ 2.0×10^{-5} s), $\boldsymbol{\zeta}$ is generated using the XORWOW[65] method for each fluid cell and particles residing in the same cell use the same fluctuation velocity to compute $\boldsymbol{u}_{Fp}$. Approximately 10^{13} random numbers are generated for each simulation. The two-way coupling between the argon bubbles and the liquid steel is incorporated by adding a source term to the liquid steel momentum equation as

$$\boldsymbol{S}_p = \sum_{i=1}^{n}\boldsymbol{S}_{p,i} = -V_{cell}^{-1}\sum_{i=1}^{n}\left(\boldsymbol{F}_{pD} + \boldsymbol{F}_{pL} + \boldsymbol{F}_{pA} + \boldsymbol{F}_{pP}\right), \quad [25]$$

where V_{cell} is the cell volume, and n is the number of the particles contained in the finite-volume cell. This approach works best when the bubbles are smaller than the cell size (4 mm), which is usually the case in this study. The effect of the argon bubbles occupying liquid steel volume is relaxed by using the volume averaged density in each cell.

An "advanced" capture criterion based on force balance is implemented to predict the capture location of the argon bubbles.[5,13,14,22] For bubbles smaller than the Primary Dendrite Arm Spacing (PDAS), the particle is assumed to enter the dendrite arms and be captured by entrapment. For bubbles larger than the PDAS, we consider eight forces acting on a spherical bubble touching three dendrite arms.[16] This capture criterion was previously applied by us in a RANS simulation of a commercial caster[4,5] with Lagrangian particle tracking model for the bubbles. The PDAS profile used in this study increases with distance down the caster from ~50 μm at the meniscus to ~200 μm at 2.5 m, as given in Fig. 3.44 in Reference 14, and is constant beyond 2.5 m. Argon bubbles that touch the SEN walls are assumed to bounce back with a 50 pct perpendicular velocity.

The above governing equations are solved with an in-house code CUFLOW[66–69] which utilizes Graphics Processing Units (GPU) to solve the equations. In CUFLOW, a fractional step method is used to solve the continuity and momentum equations. The pressure and electric potential Poisson equations are solved efficiently

Table II. Reduction of Rise Velocity with Bubble Size for Different Magnetic Field Strengths

d_p (mm)	1	2	3	4
B = 0.1 T	< 0.5 pct	1.20 pct	1.50 pct	1.70 pct
B = 0.2 T	3.60 pct	5.20 pct	6.40 pct	7.40 pct

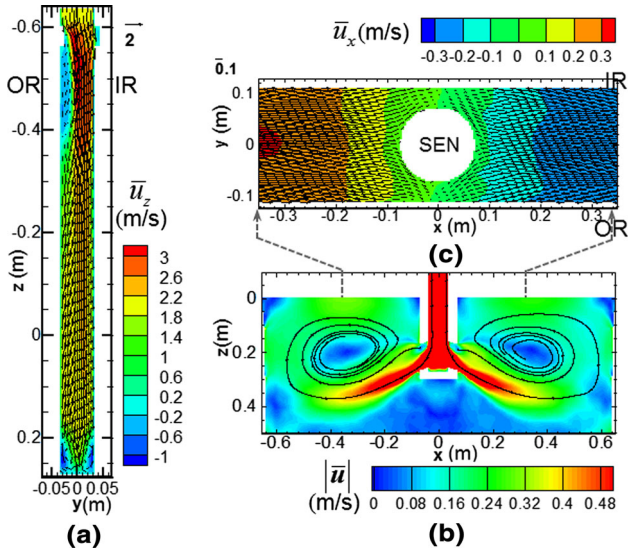

Fig. 4—Predicted time-averaged flow patterns (by LES) in the (*a*) symmetry plane of SEN, with velocity vectors and contours of *z*-velocity; (*b*) center plane of the mold with contours of velocity magnitude; (*c*) 1 cm below the meniscus region with contours of x-velocity components. Reprinted with permission from Ref. [50].

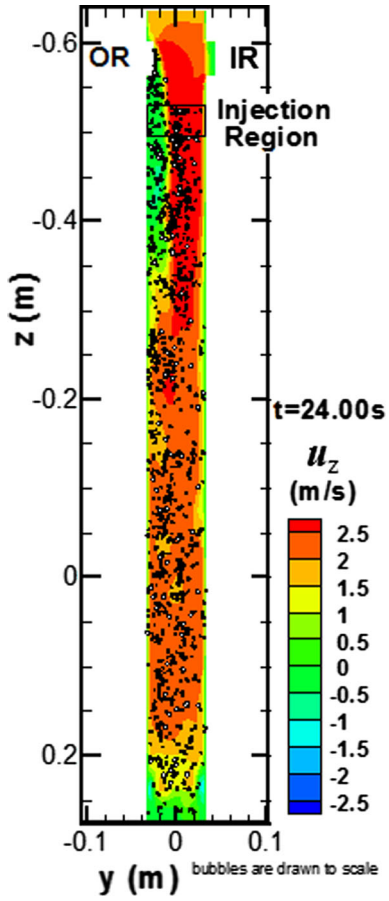

Fig. 5—Contours of *z*-velocity in the symmetry plane of SEN ($x = 0$). Argon bubbles with centers located within the region: -2 mm $< x_p < 2$ mm are shown. Reprinted with permission from Ref. [50].

by a V-cycle multigrid method, and red–black Successive Over Relaxation (SOR) with an over-relaxation parameter of 1.6. The particle transport equations are also parallelized on the GPU and solved with high efficiency. CUFLOW has been previously validated in studies of the effect of a magnetic field in a lid-driven cavity flow,[70] rise of an argon bubble in liquid steel under a magnetic field,[49] and flow in the mold region of continuous casters of steel with and without EMBr.[41,44]

III. RESULTS AND DISCUSSION

A. *Motion of the Liquid Steel*

The flow of molten steel in the mold region is critical to the final quality of the product. Figure 4[50] shows the time-averaged flow patterns in the symmetry plane of the SEN, the center plane of the mold, and a horizontal plane one cm below the top surface. The liquid steel first enters the inner-radius side of the nozzle with a maximum speed of ~ 3 m/s, forms a recirculation region ~ 0.2 m long on the outer radius side beneath the middle of the sliding plate. Two equal-sized swirls are seen at the SEN bottom. The stream traces in the center plane ($y = 0$) show a typical double-roll flow pattern. Near the top surface, the fluid moves almost parallel to the wide face with a speed of 0.25 to 0.3 m/s without any crossflow. This time-averaged flow pattern predicted using LES is different from that predicted using the RANS approach.[5] In the previous RANS simulation, the top region of each half mold contained two big eddies: one beside the SEN and the other close to the narrow face. The eddy close to the narrow face was caused by the nozzle jets impinging on the narrow face and splitting, diverting some flow upward and across the top surface toward the SEN.[5] The eddy beside the SEN disappeared in the LES simulation, presumably because the buoyancy of the argon gas is not strong enough to form a big eddy. In the RANS approach, most argon bubbles followed the time-averaged flow pattern which caused the momentum sources to be added into fewer cells that are near the SEN. The LES model computes the time-dependent behavior of the swirls at the bottom of the SEN and the unsteady swirling jets send argon bubbles to different locations at different times. The swirls inside the port predicted by RANS were from the inner radius to the outer radius, which resulted in more bubbles exiting the port near the inner radius. The buoyancy from these bubbles forms the eddy close to the SEN.

B. *Transport of Argon Bubbles*

Figure 5[50] shows contours of fluid velocity and bubble distribution (within 2 mm each side of the symmetry plane) in the symmetry plan of SEN ($x = 0$) at time $t = 24$ seconds. The bubbles are randomly injected in a cylindrical region below the slide gate with zero initial velocity. Most bubbles are carried downward by the high velocity liquid steel. In the recirculation region below the slide gate, many bubbles move up into

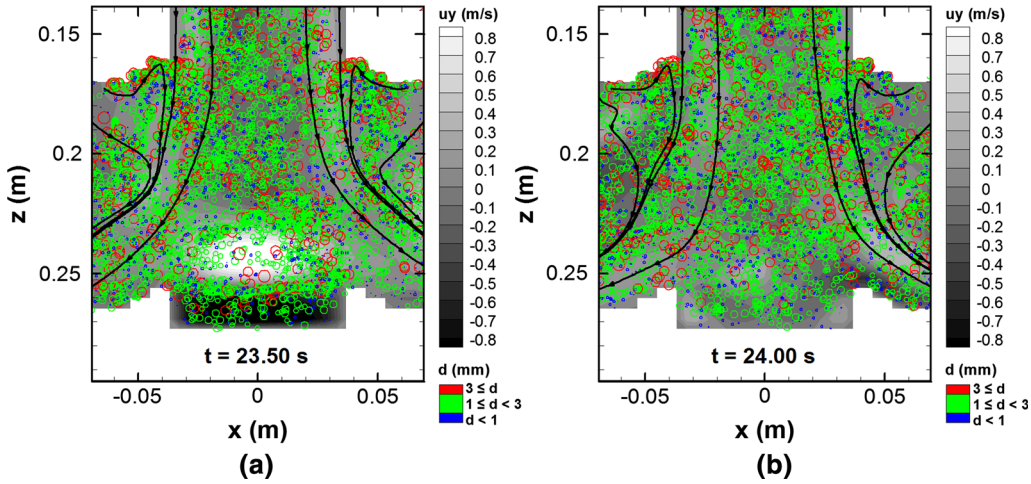

Fig. 6—Instantaneous y velocity contours (in and out of plane) and bubble locations near bottom of SEN at two different times: (*a*) 23.5 s with swirl, and (*b*) 24 s with no swirl.

the slide gate and accumulate below the mid plane of the sliding plate thus implying the formation of a gas pocket, as observed in a water experiment. The present approach cannot capture such gas pockets because of the Lagrangian approach. No bubbles were seen above the slide gate because the velocity of the downward moving steel exceeds the terminal rising velocities of the bubbles and flushes them downward.

At the bottom of the SEN, the steel jets exiting the bifurcated nozzle ports form swirls with different rotational directions, and these swirls affect the locations at which argon bubbles exit the port.[4,5,46,71] The swirl flow in the SEN also affects the bulk flow in the mold.[46,71–73] The previous RANS study[5] showed that the swirl has a downward velocity component at the inner radius, and thus most bubbles entered the mold close to the inner radius, leading to a biased capture of argon bubbles on the wide faces. However, our LES study here shows that the swirls are unsteady and frequently change their rotational direction, and sometimes two equal-sized swirls are seen. Figures 6(a) and (b) show contours of *y*-velocity in the symmetry plane at the bottom of the SEN for $t = 23.5$ and 24 seconds. At $t = 23.5$ seconds, the white spot above the bottom well of SEN shows that the flow moves from outer radius toward inner radius, due to the single large swirl of the jet. At $t = 24$ seconds, two equal-sized swirls exit the SEN ports, and no such in or out of plane bias is seen. The locations of the bubbles inside the SEN are projected onto the symmetry plane, and are colored by their diameter range. The bubbles are seen to accumulate at the top of ports and at the swirl centers. The back flow entering the top region of the ports pushes the argon bubbles into the SEN where they meet the downward-flowing jet and accumulate at the top recirculation zone of each port, where (currently not modeled) coalescence could occur. In the bottom part of the SEN, the low-pressure region of the swirl contains many bubbles, and breakup of bubbles may happen there due to the higher shear rate. When the swirls change their rotation direction, the argon bubbles at the SEN bottom are flushed into the mold region. When the swirl regions grow large enough to occupy the entire port, they bring the bubbles from the top portion of the ports to the lower high velocity exit region, from where the bubbles enter the mold region.

Figure 7 shows contours of u_x velocity in the center plane and positions of argon bubbles that are within 2 mm distance of the middle plane ($-2 < y_{\text{particle}} < 2$ mm) at time $t = 24$ seconds. The size of each argon bubble is drawn twice as big for greater clarity. Argon bubbles entering the mold are first close to each other, but due to the transient flow and the turbulence, they disperse as they are carried by the jet. The jets are close to the bottom of the two ports with a maximum speed ~ 1.7 m/s, and back flows are seen in the upper portion of the ports.

Figure 8[50] shows the region where the jet exits the nozzle port, with superimposed locations of the argon bubbles. Most bubbles enter the mold with the ~ 3 cm diameter jet at a high velocity of ~ 1.2 to 1.5 m/s. Some of these argon bubbles travel *via* backflow into the upper port. We observe that outside of the port above the jet, an eddy is shed carrying with it some large bubbles. This shedding of a vortex may be the result of a Kelvin–Helmholtz instability from the shear at the jet boundary and/or due to extra buoyancy force by a group of bubbles tearing the jet. Close to the SEN, the path lines indicate that the buoyant bubbles drive the flow up, where it meets the downward flow and forms small eddies in the upper portion of the mold. Near the top surface, most bubbles rise with a bias toward the SEN side. However, some small bubbles move downward with the liquid flow.

Figure 9 shows the distributions of bubbles at 24 seconds. In Figure 9(a), only bubbles with $d_p \geq 4$ mm are shown, while Figure 9(b) visualizes all bubbles. It can be seen that larger bubbles ($d_p \geq 4$ mm) mainly rise into the upper portion of the caster owing to larger buoyancy forces, and most bubbles smaller than 1 mm diameter are transported deep into the caster.

To quantitatively understand the size distribution of the bubbles inside the caster, the top region of the caster

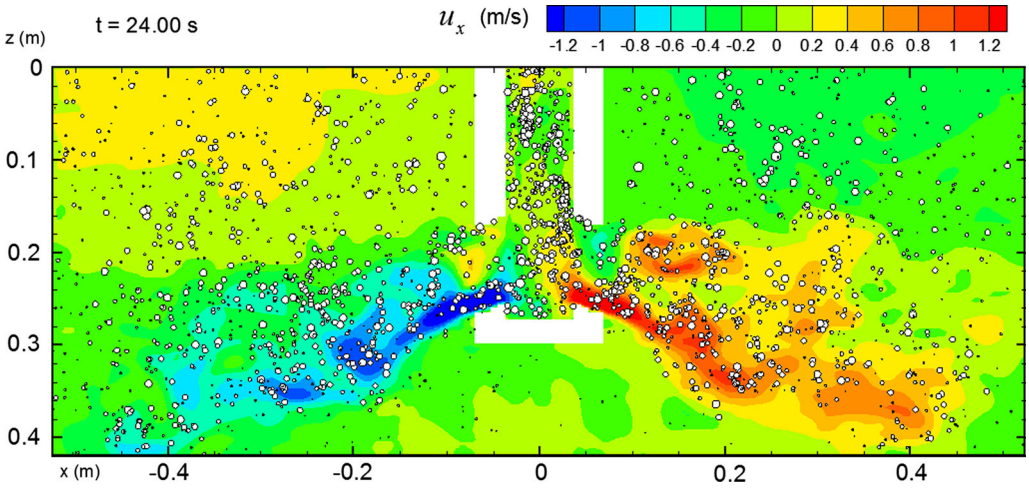

Fig. 7—Contours of u_x velocity and locations of bubbles in the middle plane ($-$ 2 mm $< y_{par} <$ 2 mm). Bubble size is drawn twice as big for greater clarity.

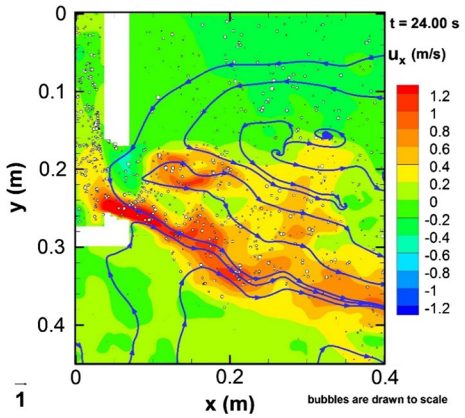

Fig. 8—Contours of u_x velocity and bubbles in the middle plane ($-$ 2 mm $< y_{par} <$ 2 mm). Reprinted with permission from Ref. [50].

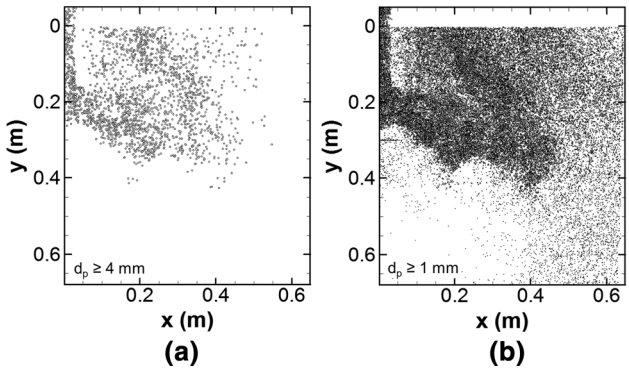

Fig. 9—Locations of bubbles inside the caster: (*a*) bubbles ≥ 4 mm, (*b*) all bubbles ≥ 1 mm.

is cut into 10 zones as shown in Figure 10. Each zone is 200 × 100 × 230 mm (height × width × thickness), and the mold thickness is also 230 mm. This figure shows the bubbles inside the caster (without EMBr) at t = 20 seconds, and the bubbles' sizes are indicated by different colors.

Figure 11 plots the size distribution of bubbles inside each zone. The number inside each subfigure indicates the zone number, and the percentage at the top shows the argon volume fraction inside each zone. The results show that in zone 6 in the jet near to the SEN, the argon volume fraction is higher (about ~ 0.88 pct), while moving toward the narrow face, the argon volume fraction reduces, to only 0.22 pct in zones 5 and 10. The size distribution in each zone is similar, as there are 800 to 1400 bubbles with sizes from 1 to 3 mm. Bubbles of other sizes are fewer than 500 in number.

Table III shows the size distribution of argon bubbles inside the caster. The results indicate that the injected bubble size distribution is different than the final distribution residing inside the caster. Although larger bubbles (*e.g.*, 26.5 pct 2 mm bubbles), were injected,

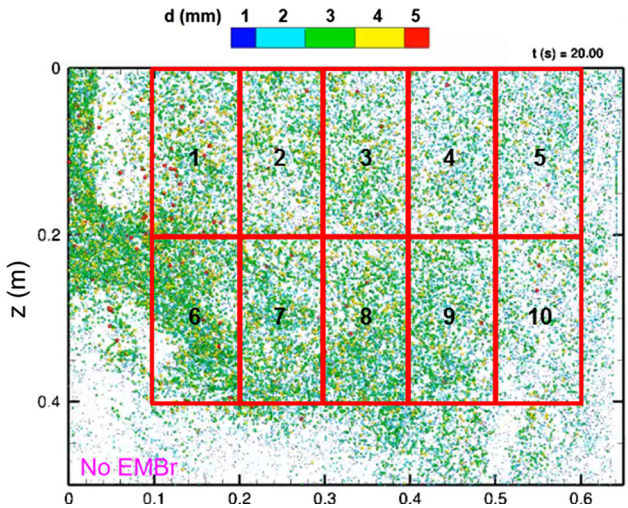

Fig. 10—Locations of bubbles inside the caster at t = 20 s without EMBr. Each zone is 200 × 100 × 230 mm (height × width × thickness).

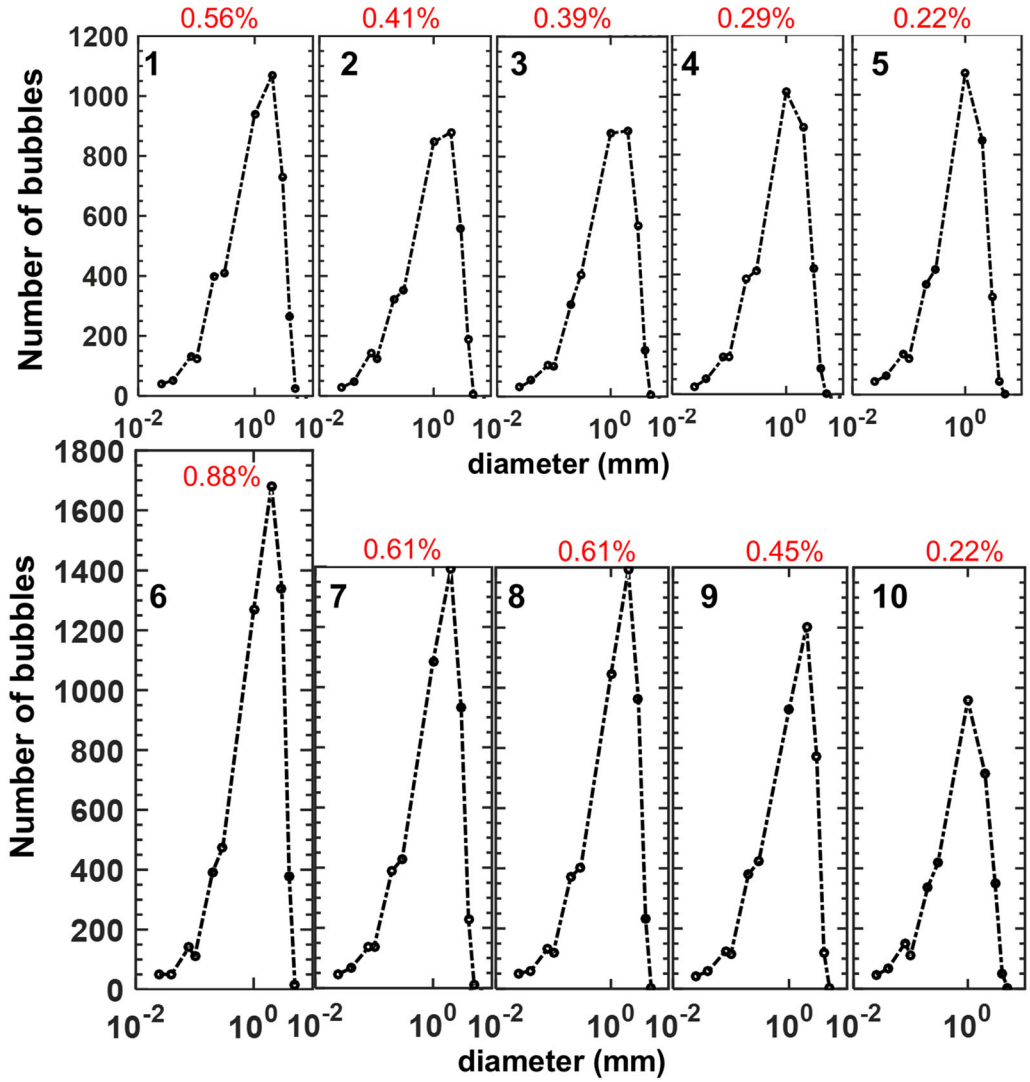

Fig. 11—Number of different bubbles inside each zone (zone numbers are shown on top of each sub figure) and the argon bubble volume fraction inside each zone.

Table III. Size Distribution of Bubbles Inside the Caster at $t = 32$ s

d_p (mm)	0.025	0.04	0.08	0.1	0.2	0.3	1	2	3	4	5
Injected (pct)	0.49	0.74	1.47	1.23	3.69	4.67	19.41	33.17	26.54	8.11	0.49
Remaining (pct)	1.89	2.80	5.74	5.20	15.78	17.50	23.69	15.39	9.46	2.41	0.12

only ~ 10 pct of the bubbles in the mold have 2 mm diameter. Similarly, only 0.5 to 5 pct of small bubbles are injected, but 3 to 17 pct of these small bubbles reside inside the caster after 32 seconds. The present study does not include bubble break up or coalescence; hence this result is solely caused by the different residence times of the bubbles: larger bubbles tend to leave from the domain much quicker than smaller bubbles, while smaller bubbles travel with the fluid for a longer time before they escape from the top surface or are captured by the shell.

C. *Capture and Removal of Argon Bubbles*

An important issue during continuous casting of steel is the capture and removal of argon bubbles. Argon bubbles may escape into the top slag layer, or be captured by the insides of the solidifying shell, where they often form defects. It is important to understand the transport and interaction of the bubbles with the steel shell to understand the formation of defects in the cast steel. Therefore, during our simulations, bubbles were continually injected into the domain at a rate of

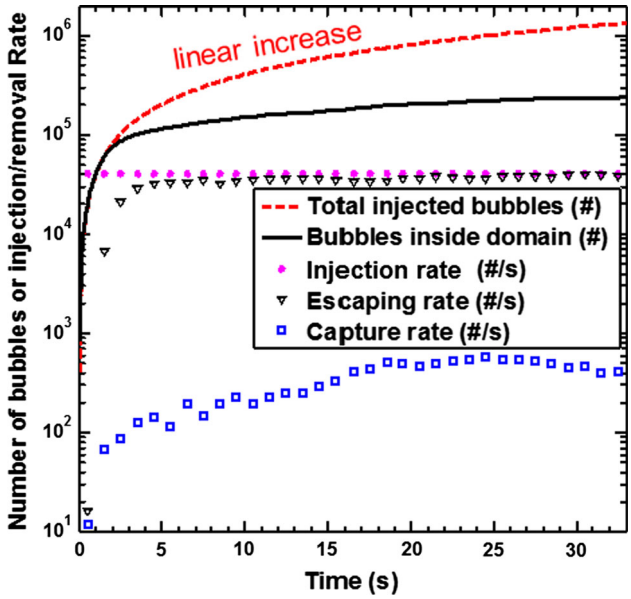

Fig. 12—History of number of injected particles, injection rate, removal rate (particles that escaped from top surface), and capture rate (captured by shell). Reprinted with permission from Ref. [50].

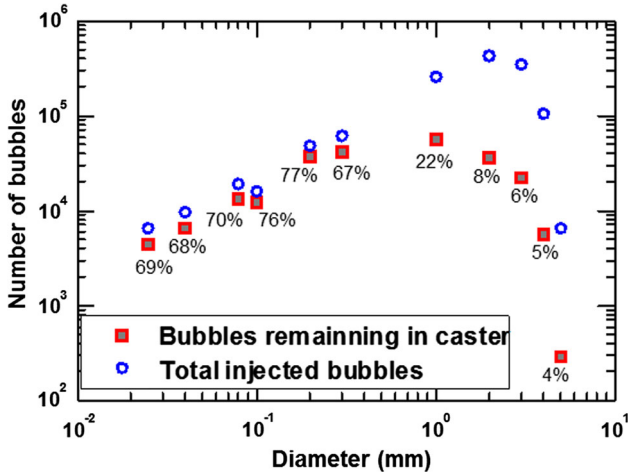

Fig. 13—Statistics of bubbles inside the caster (without EMBr). Reprinted with permission from Ref. [50].

40,700 particles per second (8.2 pct by volume). Figure 12[50] shows how these various contributions to the particle number evolve over time inside the caster. As particles are continually injected, a large number of particles escape from the top. Some are captured by the shell, as shown in the figure. The rest of the particles reside in the domain to be captured or to escape at later times. After 30 seconds, the total number of bubbles inside the domain does not change much, and the escape plus capture rates roughly equal the injection rate, so a quasi-steady state condition has been reached. At this time, the capture rates are 400 to 600 bubbles per second, which is about 100 times smaller than the injection rate, indicating an overall capture fraction of ~ 1 pct.

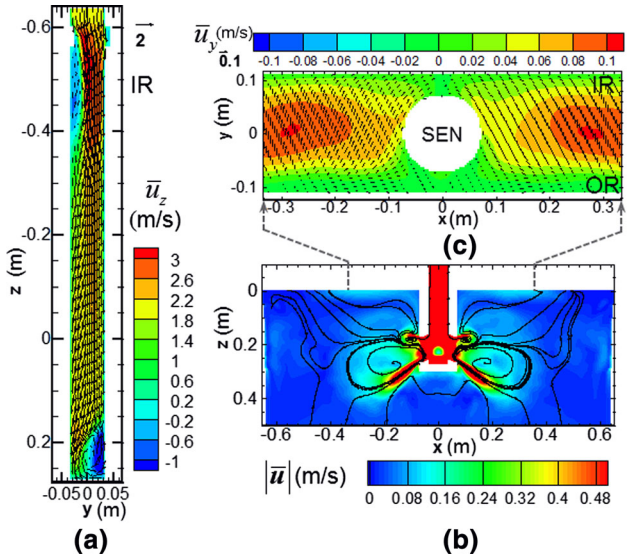

Fig. 14—Predicted flow patterns in the (*a*) symmetry plane of SEN, with velocity vectors and contours of *z*-velocity; (*b*) center plane of the mold with contours of velocity magnitude; (*c*) a plane 1 cm below the meniscus region with contours of *y*-velocity components with EMBr.

Figure 13[50] shows the number of bubbles remaining in the domain versus the size of the bubbles. For bubbles with $d_p \leq 0.3$ mm, the number of bubbles remaining inside the domain is nearly proportional to the number of bubbles injected into the domain. However, the number of large bubbles remaining in the caster is much less than injected, owing to their high escape rate. The percentages shown in the figure indicate the fraction of bubbles remaining in the caster, for each size. The fraction of large bubbles (> 1 mm) remaining in the domain is small (4 to 22 pct) as most of them escape from the top surface. On the other hand, most (68 pct) small bubbles ($d_p \leq 0.1$ mm) remain in the domain, with the rest being easily captured because they are smaller than the PDAS. Approximately 77 pct of bubbles between 0.1 and 0.2 mm diameter remain in the domain as they are neither able to escape to the top nor be captured by the shell due to their larger size.

D. *Effects of EMBr on Flow Field and Argon Bubble Transport*

Applying a magnetic field affects the time-averaged flow behavior in the caster as well as the transient flow structures.[40,41,44,45] It also reduces the mean surface velocity and fluctuations[18,38–42,44,45] at the slag/steel interface. Figure 14 shows the time-averaged flow fields in the nozzle, at the center of the mold, and at 1 cm below the top surface. Figure 14(a) shows that in the upper portion of nozzle, the flow field is similar to that without the EMBr because of the locally weak magnetic field. A big counterclockwise rotating swirl (with downward velocity near outer radius) is seen at the bottom of the nozzle which is different from two equal-sized swirls seen in the zero-magnetic field case. In both cases, the steel flow first enters the inner-radius side of the SEN

and is then deflected to the outer-radius side. With the application of the magnetic field, the induced Lorentz force reduces the fluctuations inside the SEN and makes the counterclockwise rotation dominate at the bottom. As shown in Figure 14(b), in the mold region, the velocity is much smaller than that without the EMBr. The upper rolls are closer to the jets which are also thinner and shorter. Near the top of the ports, two recirculation zones are formed due to the buoyancy of the exiting argon bubbles. Figure 14(c) shows a top view just below the top surface, revealing a crossflow (~ 0.1 m/s) from the outer radius toward the inner radius. The formation of this crossflow is due to the strong counterclockwise rotating swirls inside the SEN which send most argon bubbles to the outer radius side of the mold.

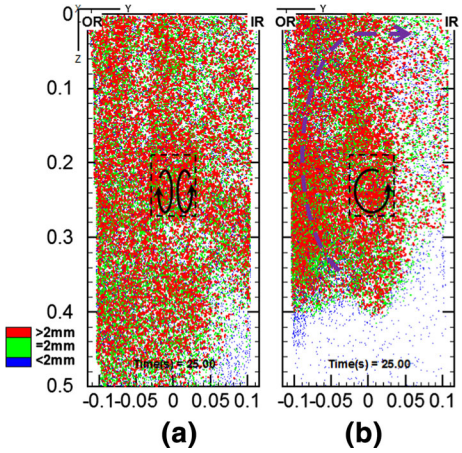

Fig. 15—Side projection view from the narrow face of all bubbles inside the caster. (*a*) without EMBr and (*b*) with EMBr. The dashed square indicates the port location, and the black arrows show the swirl inside the port.

Figure 15 compares side views of the bubble distribution inside the mold with and without the EMBr. As shown in Figure 15(a), without EMBr, bubbles are sent deeper into the mold, with roughly uniform distribution between inner and outer radii. However, with the EMBr, Figure 15(b) shows that more bubbles are sent to the outer radius of the mold, owing to the single counterclockwise swirl of the jet exiting the nozzle. These bubbles rise in the region of the outer-radius side of the mold and induce small crossflow near the top surface.

Figure 16 shows the wide face projection views of all bubbles inside the caster, for cases with and without EMBr, respectively. The diameter of bubbles is indicated using different colors. The animations (from t = 15 to 25 seconds) are available as supplementary materials. The results show that with EMBr, fewer bubbles are sent to deeper regions of the caster, and fewer bubbles are carried to the narrow face. The magnetic field strengths near the dashed lines are labeled in Figure 16, because the different magnetic field strengths slow down the argon bubbles differently. The percentages of reduction in velocities are also labeled in Figure 16. The bubbles rise much slower when compared with the case without EMBr because the flow is much slower when EMBr is used and the drag coefficient is higher in the presence of the magnetic field.

E. *Effect of EMBr on Argon Bubble Capture and Removal*

Figures 17(a) through (c) show the locations of all bubbles captured during the entire simulation on the inner and outer radii of the wide face and on the narrow face with EMBr. Compared with the case without EMBr (Figure 25, which will be discussed later), the EMBr causes more bubbles to be captured in the upper portion of the mold and less bubbles captured in the lower

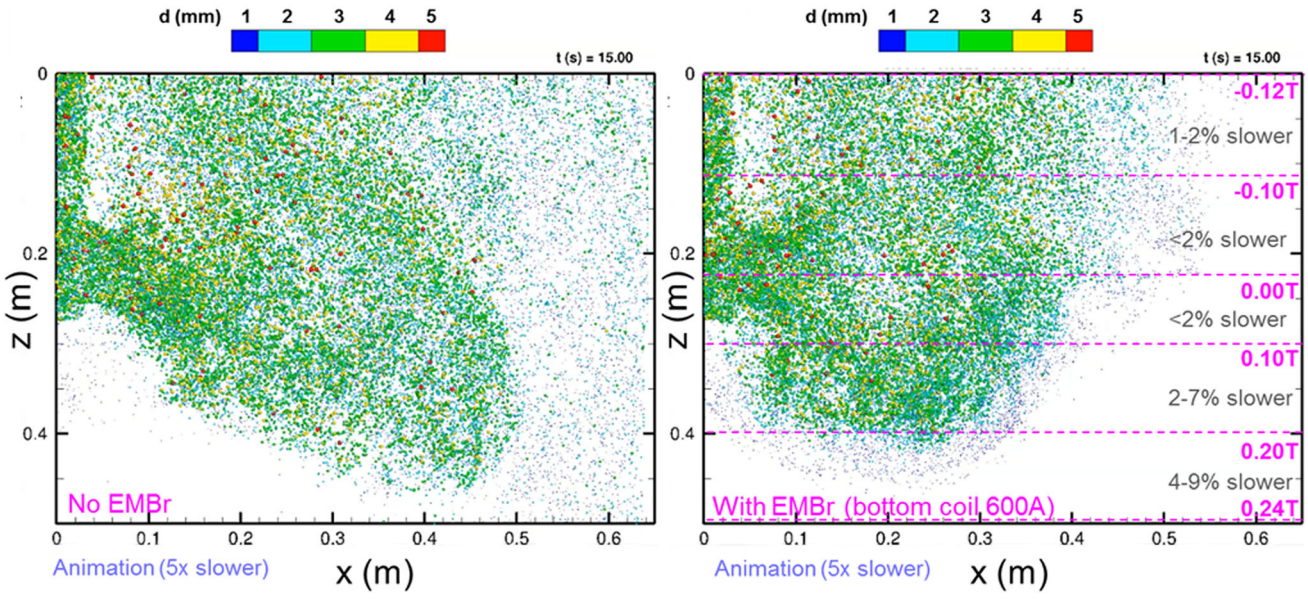

Fig. 16—Snapshot of front projection of all the bubbles inside the caster with and without EMBr. (Animations are available as supplementary material).

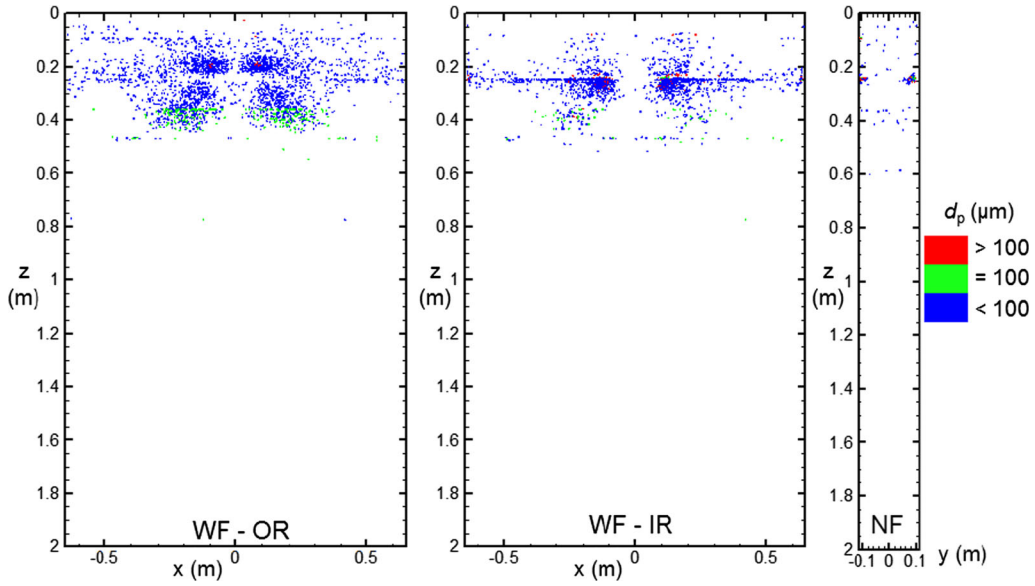

Fig. 17—Bubbles captured (0 to 30 s) by the solidifying shell for case with EMBr. From left to right: wide face outer radius, wide face inner radius, and narrow face.

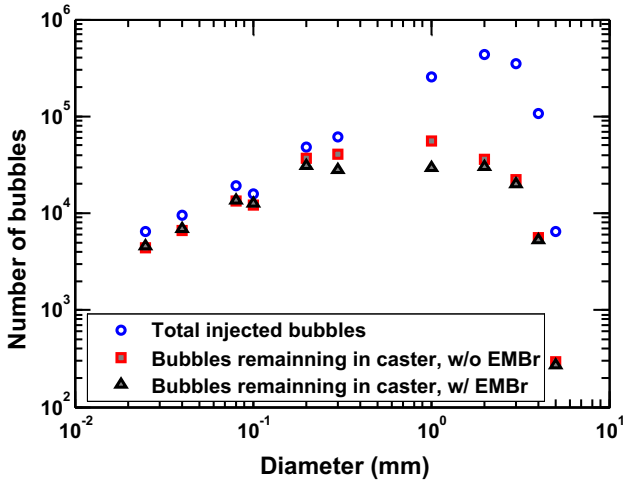

Fig. 18—Total injected bubbles and bubbles remaining inside the caster.

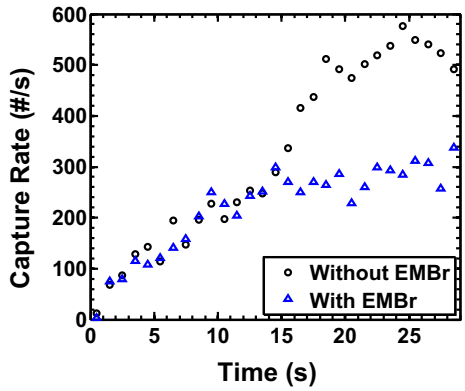

Fig. 19—Total capture rate of bubbles for case with and without EMBr.

sections. Most of the captured bubbles are smaller than 100 μm diameter (blue), and no bubbles larger than 1 mm are captured. The total number of captured bubbles is also much less with EMBr.

Using EMBr also lowers the number of bubbles remaining inside the caster. Figure 18 shows the effect of EMBr on bubble size population inside the caster at t = 29 second. The number of injected bubbles of each size in the distribution are shown with blue circles, and is the same for both cases (with and without EMBr). For small bubbles ($d_p \leq 0.1$ mm), about 70 pct remain inside the caster for both cases. After applying the magnetic field, the number of medium-sized bubbles ($0.2 \leq d_p \leq 1$ mm) inside the caster are reduced. This is because the Lorentz force changes the flow pattern and suppresses turbulence and velocity fluctuations, which prevents these mid-sized bubbles from moving deep in the mold, thereby shortening their residence times in the caster. The EMBr has a smaller effect on the larger bubbles (diameter greater than 2mm) because the buoyancy forces on these bubbles are quite large, so most of them float quickly to the top surface, in both cases.

The total capture rate of argon bubbles decreases significantly using EMBr. Figure 19 compares the total bubble capture rate for both cases. Without EMBr, the capture rate fluctuates between 400 and 600 bubbles per second after 20 seconds. With EMBr, the capture rate drops by a factor of two, fluctuating between 200 and 300 bubbles per second. This is likely due in part to EMBr suppressing the unsteady swirl, (see Figure 15b) shortening jet penetration, and exerting larger drag forces on the bubbles. Thus, fewer bubbles are sent toward the narrow face, which lowers their capture rate. EMBr also reduces turbulent fluctuations and slows down the steel inside the caster, which causes fewer

bubbles to be transported to deeper regions in the caster, where capture is easier. Most bubbles float upward and escape at the top surface. It is important to note that EMBr affects the capture rate mainly by modifying the flow field. It is hard to conclude that EMBr always reduces the capture rate.

In general, EMBr greatly lowers the capture rates and fractions of bubbles, especially for medium-sized bubbles. Figures 20(a) and (b) compare the fractions and rates of capture of different size bubbles with and without EMBr. Without EMBr, the capture fraction of very small bubbles ($d_p \le 0.08$ mm) is around 35 pct, and turning on EMBr reduces this to around 25 pct. The effect of EMBr on the capture of 0.1 mm bubbles is even more significant. EMBr reduces the capture fraction for this medium size from ~ 20 pct to only ~ 4 pct. This is because EMBr reduces the transport of bubbles to deeper regions within the caster, where the PDAS is large, and can easily capture these bubbles. The capture fraction of larger bubbles (0.2 and 0.3 mm diameter) is only ~ 1 pct for both cases. Capture rates follow the same trends. Figure 20(a) shows that when no EMBr is applied, the capture rate of small bubbles with $d_p \le 0.1$ mm is between 50 and 200 bubbles per second. Using EMBr significantly reduces these capture rates.

F. *Comparisons with Previous RANS Results*

Figure 21 compares the capture fractions of different bubble sizes with results of a previous study using a RANS model.[5] The RANS simulations used a random walk model for the particle dispersion and predicted that about 85 pct of bubbles with $d_p \le 0.1$ mm are captured. This is a significantly larger fraction than that predicted by the LES model (~ 25 pct). These small bubbles are much smaller than the PDAS and therefore get captured when they touch the surface. Therefore, the observed difference is caused primarily by the different flow fields and the behavior near the domain boundaries. The random walk model overpredicts the capture of small bubbles due to its assumption of isotropic turbulence which generates a relatively larger velocity fluctuation component normal to the wall than predicted using LES. For small bubbles ($0.2 \le d_p \le 0.3$ mm), the LES predicts a capture fraction of 1 pct, which again is much lower than that predicted using the RANS approach. Bubbles larger than 1 mm in diameter are not captured in this study.

Figure 22 compares the predicted capture rate with previous RANS predictions.[5] The LES predicts the capture rate of very small bubbles ($d_p \le 0.1$ mm) to be 75 to 200 bubbles per second, while 180 to 400 bubbles per second were captured with the RANS model. The capture rate of small bubbles ($0.2 \le d_p \le 0.3$ mm) is between 10 and 20 bubbles per second, which is about 50 to 100 times smaller than that predicted by RANS. The RANS simulation predicted that the capture rate of 1 mm bubbles is about 10 bubbles per second, but bubbles larger than 1 mm diameter were not captured in the LES. This is likely due to the RANS random walk method overprediction of velocity variations toward the solidification front, associated with its assumption of isotropic turbulence even in the boundary layer region.

Figure 23[50] shows the predicted average bubble diameter beneath the strand of the narrow face surface and the inner radius of the wide face. These results are compared with both RANS predictions and plant

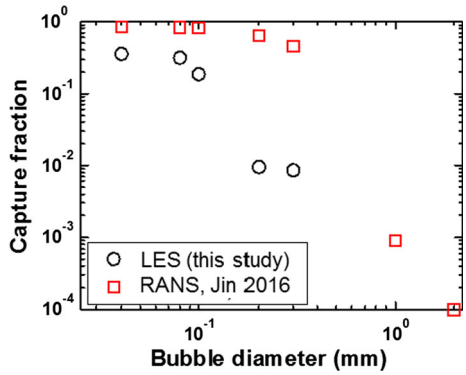

Fig. 21—Capture fraction of bubbles of different size, compared with previous RANS results.

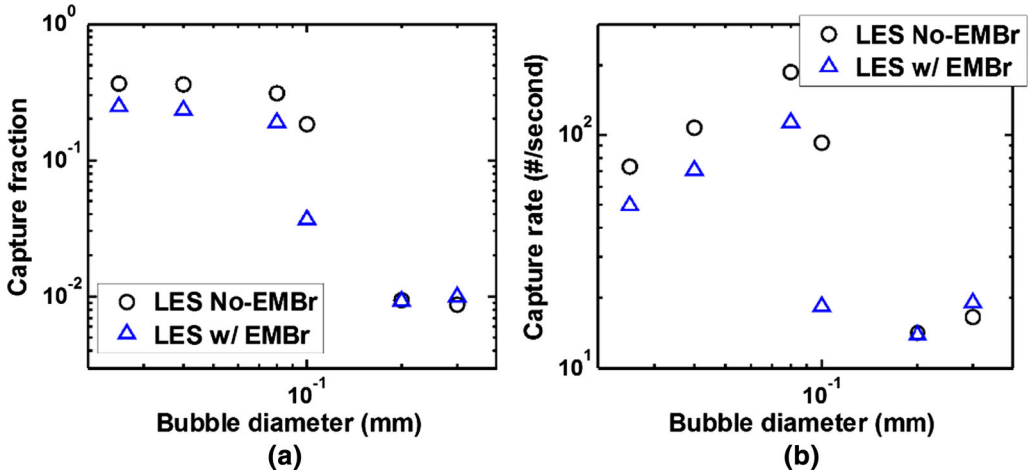

Fig. 20—Effect of EMBr on (*a*) capture fractions and (*b*) capture rates of bubbles.

measurements.[4,5] The star symbols show the results of RANS model with a simple capture criterion which assumes "touch is captured" for all bubbles. This criterion greatly over predicts the average bubble diameter captured. Using the advanced capture criterion with RANS[13,14,16] the predictions agree better with the measurements, but still predict a larger average bubble diameter. This is likely due to the overprediction of the capture of smaller bubbles ($0.2 \leq d_p \leq 0.3$ mm) as mentioned earlier. Using the LES approach, the predicted average bubble diameter is closer to that measured at Baosteel.[4,5] Similar results are seen for the inner radius of the wide face. Figure 23(b) shows the average diameter of bubbles obtained from a sample cut from the center region of the inner radius of the wide face, and the results from both RANS and LES simulations. LES predicted the average bubble diameter to be ~ 0.1 mm which matches better with the measurements. However, both models predict that no bubbles are captured near the strand surface, which corresponds to solidification near the meniscus region. One possible reason for this discrepancy may be that hooks are not included in the models, but hooks are known to capture bubbles close to the meniscus.[74]

Figure 24 compares the predicted number of bubbles captured in each sample layer with previous measurements and RANS results. Figure 24(a) shows that both RANS and LES predict fewer bubbles captured than

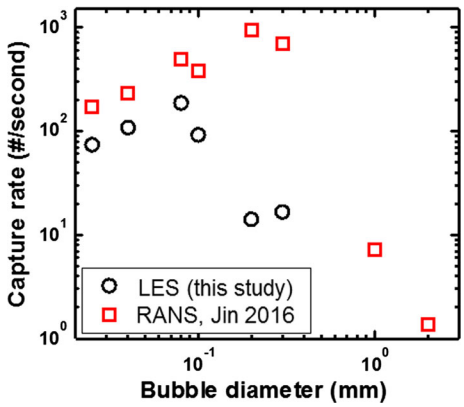

Fig. 22—Capture rate of bubbles of different sizes.

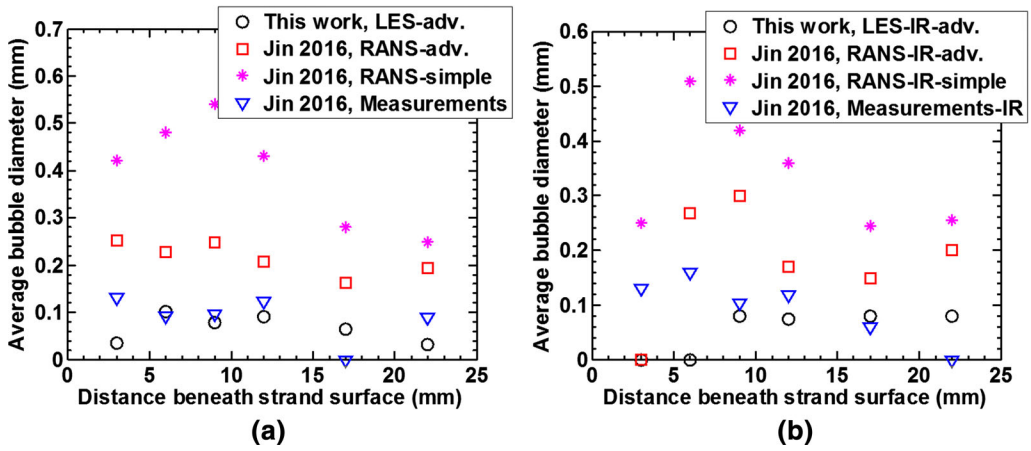

Fig. 23—Comparisons of predicted average bubble diameter on each sample layer on (*a*) NF and (*b*) WF-IR sample with previous RANS simulation and measurements. Reprinted with permission from Ref. [50].

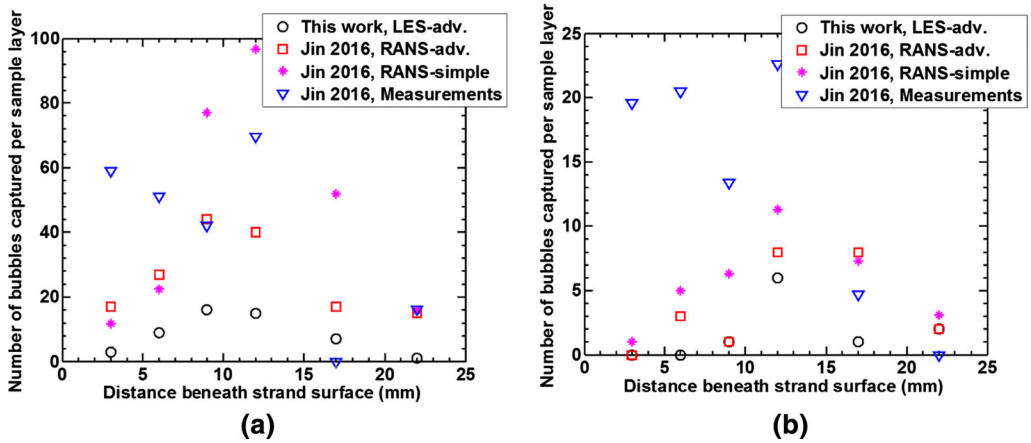

Fig. 24—Comparisons of predicted number of captured bubbles on each sample layer on (*a*) NF and (*b*) WF-IR sample with previous RANS simulation and measurements.

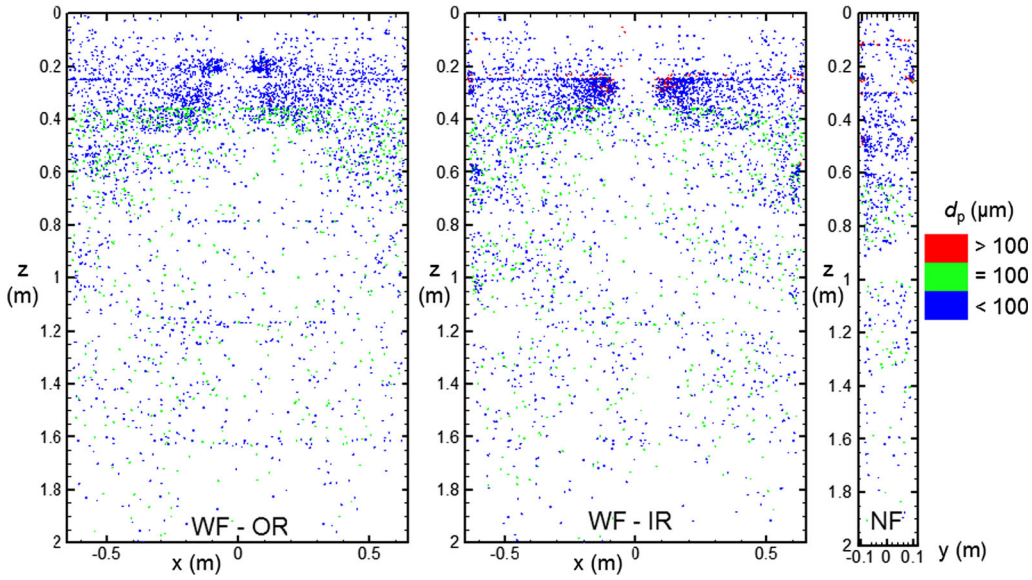

Fig. 25—Bubbles captured by the solidifying shell without EMBr. From left to right: outer radius of wide face, inner radius of wide face, and narrow face. Note no bubble larger than 1 mm is captured.

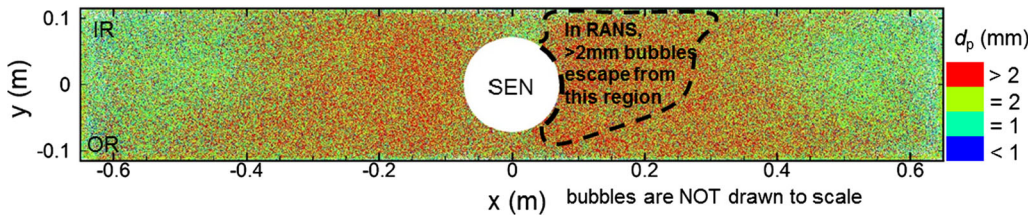

Fig. 26—The escape location of bubbles from the top surface. This relatively uniform distribution contrasts with RANS model's predictions that bubbles > 2 mm diameter only escape near the SEN.

found in the measurements, especially near the strand surface. LES predicts even fewer captured bubbles than the RANS model. Similar trends are found for the narrow-face and wide-face samples and predictions. This mismatch may due to the bubble size distribution. For a given gas volume fraction, if the size distribution contains more small bubbles than large bubbles, then more bubbles will be captured. Thus, perhaps the injected bubble size distribution assumed in these studies was skewed to have too few small bubbles. These results suggest that more research is needed to investigate the bubble size distribution in the caster.

Figure 25 shows bubbles captured by the shell without EMBr during the time interval $11 < t < 33$ seconds. These small bubbles are captured deep in the caster, which agrees with previous studies.[5,15,21,24] We compute that 3196 and 3672 bubbles are captured by the outer and inner wide faces, respectively. The prediction of more bubbles captured by the inner side than the outer side agrees with the previous RANS model,[4,5] although the LES predicts a much smaller capture rate. Each narrow face captures ~ 600 bubbles which is 5 to 6x less bubbles than captured by the wide face, and is roughly proportional to the surface area. This is different from the RANS results which predicted a similar capture rate on the narrow face and outer radius of wide face. The slight banding effect is due to the staircase mesh of the shell and should be ignored.[13,31] No bubbles larger than 1 mm are captured during the LES simulation. On the inner radius, more 200 and 300 μm bubbles are captured in the central region of the inner-radius wide face, near to the port exits. Although they can be captured almost anywhere, more 100 μm bubbles are captured in the upper region of the mold near the port exits. Only a few bubbles are captured in the top center region between the SEN and the wide face, because most small bubbles follow the jet, so their chances to enter this region are low. On the wide face, most 100 μm bubbles are captured ~ 0.4 m below the top surface (~ 2 cm beneath the strand surface) and ~ 0.65 m, because the PDAS is larger than the bubbles size (easy for bubbles to enter between the dendrite arms), and the high-speed swirling jet-induced turbulence increased the chance of bubbles to reach shell.

Figure 26 shows the distribution of all bubbles that escaped from the top surface during $11 < t < 33$ seconds. Larger bubbles (≥ 3 mm) escape close to the SEN, but the 1- and 2-mm-sized bubbles escape from anywhere on

the top surface. Both the current LES and a previous RANS model[5] show that bubbles with $d \geq 3$ mm leave close to SEN and are biased toward the inner radius of the caster, while fewer bubbles escape from the region between the SEN and wide faces. However, the RANS model predicts that these bubbles escape within ~ 0.3 m away from the SEN center (the region enclosed by the dashed line), while the LES model shows they leave within 0.5 m away from the SEN center. This may be because the RANS model does not predict the transient oscillation of the jet which sends the bubbles to farther locations.

IV. CONCLUSIONS

Two-phase turbulent flow and capture of argon bubbles is simulated inside a commercial steel caster with and without the use of an EMBr magnetic field, using LES and a coherent-structure subgrid-scale model. The effect of Lorentz force on bubble drag is included by modifying the drag coefficient. An advanced force balance capture criterion[13,14,16] was used to predict the capture of argon bubbles in the solidifying dendritic interface. The important findings of this study are summarized below:

1. With a casting speed of 1.5 m/min and 8 pct argon gas (hot), a classic double-roll flow pattern is seen when EMBr is turned off. The buoyancy forces of bubbles are not strong enough to cause reverse flow (from SEN to NF) on top surface. This flow pattern is somewhat different from a previous study using a RANS model.[5]
2. Without EMBr, the RANS approach predicts that most of the large bubbles escape very near to the nozzle (< 0.3 m away from SEN center), while LES shows that the transient turbulent jets can sporadically send larger bubbles further toward the narrow face. The wider, more uniform size distribution of argon bubbles reduces the buoyancy effect of the bubbles in the near-SEN region, so no reverse flow is seen.
3. The Lagrangian approach predicts that the bubbles accumulate in the reverse flow region beneath the slide gate and at the top of the ports, which agrees with water model experiments. Accumulation of argon bubbles is also seen in the low-pressure region of the vortex center at the bottom of the SEN.
4. Although the gas injection volume fraction is ~ 8 pct, the volume fraction remaining inside most of the mold region of the caster is less than 1 pct. The volume fraction of bubbles is even less near the narrow face.
5. The size distribution of argon bubbles inside the caster is quite different from the injected bubble distribution, due to the different residence times of the bubbles. Calculations here show that the fraction of small bubbles (0.025 to 0.3 mm) is three times larger than the initial injection fraction, while the fractions of large bubbles (2 to 5 mm in diameter) are 2 to 4 times smaller than their injected fractions. The fraction of 1 mm bubbles remaining in the mold is only ~ 19 pct of the injected fraction.
6. Without EMBr, the LES model predicts that a smaller number of bubbles are captured (only 1 pct) compared with a RANS model[5] (~ 60 pct), especially for $0.2 \leq d_p \leq 0.3$ mm bubbles. The causes for this discrepancy might be (1) the different flow patterns predicted by the two models; and (2) the use of random walk with isotropic turbulence in the RANS model which overpredicts the chance of bubbles hitting the walls.
7. Both LES and RANS models predict that large bubbles (> 2 mm) are not captured. The LES model predicts that the average diameter of captured argon bubbles is ~ 0.1 mm which matches well with measurements.[4,5]
8. Without the EMBr, the LES simulation shows two equal-sized swirls at the bottom of SEN. However, with EMBr, only a counterclockwise swirl is seen at the bottom of the SEN. This dominating swirl causes more bubbles to go toward the outer-radius side of the mold and leads to crossflow near the top surface.
9. EMBr reduces the penetration depth of the two jets exiting from the ports. A smaller number of bubbles are sent to the narrow face and not sent deep into the caster. This causes a smaller number of bubbles to be captured for the conditions studied here. The total capture rate reduces from 500 to 600 bubbles per second to 200 to 300 bubbles per second when EMBr is applied.
10. EMBr significantly lowers the capture rate and capture fraction of small bubbles for the conditions studied here. For tiny bubbles, using EMBr reduces the capture rate from 75 to 50 bubbles per second, and the capture fraction reduces from ~ 35 to ~ 25 pct. For 0.1 mm bubbles, using EMBr reduces the capture rate from 100 to 20 bubbles per second. The capture rate of larger bubbles of sizes 0.2 and 0.3 mm ranges only from 15 to 20 bubbles per second both with and without EMBr.

ACKNOWLEDGMENTS

The authors gratefully acknowledge the financial supports from the National Science Foundation (Grant No. CMMI 15-63553) and the Continuous Casting Consortium, the Univ. of Illinois at Urbana-Champaign. Thanks to Baosteel, Shanghai, P.R. China for providing the casting conditions and measurements. This research is also part of the Blue Waters sustained-petascale computing project, which is supported by the National Science Foundation (Awards OCI-0725070 and ACI-1238993) and the State of Illinois. Blue Waters is a joint effort of the University of Illinois at Urbana-Champaign and its National Center for Supercomputing Applications. The authors also thank NVIDIA Hardware Grant Program for providing the GPUs for an in-house workstation.

ELECTRONIC SUPPLEMENTARY MATERIAL

The online version of this article (https://doi.org/10.1007/s11663-018-1191-1) contains supplementary material, which is available to authorized users.

REFERENCES

1. H. Bai and B.G. Thomas: *Metall. Mater. Trans. B*, 2001, vol. 32, pp. 253–67.
2. H. Bai and B.G. Thomas: *Metall. Mater. Trans. B*, 2001, vol. 32, pp. 707–22.
3. K.G. Rackers and B.G. Thomas: in *78th Steelmaking Conference Proceedings*, Iron and Steel Society, Nashville, TN, 1995, pp. 723–34.
4. K. Jin, B.G. Thomas, R. Liu, S.P. Vanka, and X.M. Ruan: *IOP Conf. Ser. Mater. Sci. Eng.*, 2015, vol. 84, p. 012095.
5. K. Jin, B.G. Thomas, and X. Ruan: *Metall. Mater. Trans. B*, 2016, vol. 47, pp. 548–65.
6. L. Zhang, J. Aoki, and B.G. Thomas: *Metall. Mater. Trans. B*, 2006, vol. 37, pp. 361–79.
7. H.L. Yang, P. He, and Y.C. Zhai: *ISIJ Int.*, 2014, vol. 54, pp. 578–81.
8. B.G. Thomas and X. Huang: in *76 th Steelmaking Conference*, 1993, pp. 273–89.
9. B.G. Thomas, X. Huang, and R.C. Sussman: *Metall. Mater. Trans. B*, 1994, vol. 25, pp. 527–47.
10. C. Pfeiler, M. Wu, and A. Ludwig: *Mater. Sci. Eng. A*, 2005, vol. 413, pp. 115–20.
11. Y. Wang and L. Zhang: *Metall. Mater. Trans. B*, 2011, vol. 42, pp. 1319–51.
12. Q. Yuan, B.G. Thomas, and S.P. Vanka: *Metall. Mater. Trans. B*, 2004, vol. 35, pp. 703–14.
13. Q. Yuan: Ph.D. Thesis, University of Illinois at Urbana-Champaign, 2004.
14. S. Mahmood: MS Thesis, University of Illinois at Urbana-Champaign, 2006.
15. L. Zhang and Y. Wang: *JOM*, 2012, vol. 64, pp. 1063–74.
16. B.G. Thomas, Q. Yuan, S. Mahmood, R. Liu, and R. Chaudhary: *Metall. Mater. Trans. B*, 2014, vol. 45, pp. 22–35.
17. V. Singh, S.K. Dash, J.S. Sunitha, S.K. Ajmani, and A.K. Das: *Isij Int.*, 2006, vol. 46, pp. 210–8.
18. B. Li, T. Okane, and T. Umeda: *Metall. Mater. Trans. B*, 2000, vol. 31, pp. 1491–503.
19. R. Sanchez-Perez, L. García-Demedices, J.P. Ramos, M. Diaz-Cruz, and R.D. Morales: *Metall. Mater. Trans. B*, 2004, vol. 35, pp. 85–99.
20. Z. Liu, F. Qi, B. Li, and M. Jiang: *Metall. Mater. Trans. B*, 2015, vol. 46, pp. 933–52.
21. R.C. Sussman, M.T. Burns, X. Huang, and B.G. Thomas: in *10th Process Technology Conference Proceedings.*, vol. 10, Iron and Steel Society, Toronto, Ontario, 1992, pp. 291–304.
22. Q. Yuan and B.G. Thomas: in *Third Int. Congress on Science and Technology of Steelmaking*, 2005, pp. 745–62.
23. C. Pfeiler, B.G. Thomas, M. Wu, A. Ludwig, and A. Kharicha: *Steel Res. Int.*, 2008, vol. 79, pp. 599–607.
24. C. Liu, Z. Luo, T. Zhang, D. Shen, W. Nan, and Z. Zou: *J. Iron Steel Res. Int.*, 2014, vol. 21, pp. 403–07.
25. Z. Liu, B. Li, M. Jiang, and F. Tsukihashi: *ISIJ Int.*, 2013, vol. 53, pp. 484–92.
26. B.G. Thomas, A. Denissov, and H. Bai: in *Steelmaking Conference Proceedings*, vol. 80, IRON AND STEEL SOCIETY OF AIME, 1997, pp. 375–84.
27. E. Krepper, D. Lucas, T. Frank, H.-M. Prasser, and P.J. Zwart: *Nucl. Eng. Des.*, 2008, vol. 238, pp. 1690–1702.
28. Z.Q. Liu, F.S. Qi, B.K. Li, and S.C.P. Cheung: *Int. J. Multiph. Flow*, 2016, vol. 79, pp. 190–201.
29. R.C. Sussman, M.T. Burns, X. Huang, and B.G. Thomas: *Iron Steelmak.*, 1993, vol. 20, pp. 14–16.
30. Z. Liu, B. Li, and M. Jiang: *Metall. Mater. Trans. B*, 2014, vol. 45, pp. 675–97.
31. Q. Yuan, B.G. Thomas, and S.P. Vanka: *Proc. Process Technol. ISSTech*, 2003, pp. 913–27.
32. K. Takatani, K. Nakai, N. Kasai, T. Watanabe, and H. Nakajima: *ISIJ Int.*, 1989, vol. 29, pp. 1063–68.
33. D.-S. Kim, W.-S. Kim, and K.-H. Cho: *ISIJ Int.*, 2000, vol. 40, pp. 670–76.
34. K. Cukierski and B.G. Thomas: *Metall. Mater. Trans. B*, 2008, vol. 39, pp. 94–107.
35. H. Yu, B. Wang, H. Li, and J. Li: *J. Mater. Process. Technol.*, 2008, vol. 202, pp. 179–87.
36. H. Harada, T. Toh, T. Ishii, K. Kaneko, and E. Takeuchi: *ISIJ Int.*, 2001, vol. 41, pp. 1236–44.
37. X. Miao, K. Timmel, D. Lucas, Z. Ren, S. Eckert, and G. Gerbeth: *Metall. Mater. Trans. B*, 2012, vol. 43, pp. 954–72.
38. Z.-D. Qian and Y.-L. Wu: *ISIJ Int.*, 2004, vol. 44, pp. 100–07.
39. Y.-S. Hwang, P.-R. Cha, H.-S. Nam, K.-H. Moon, and J.-K. Yoon: *ISIJ Int.*, 1997, vol. 37, pp. 659–67.
40. R. Singh, B.G. Thomas, and S.P. Vanka: *Metall. Mater. Trans. B*, 2013, vol. 44, pp. 1201–21.
41. R. Chaudhary, B.G. Thomas, and S.P. Vanka: *Metall. Mater. Trans. B*, 2012, vol. 43, pp. 532–53.
42. A. Idogawa, M. Sugizawa, S. Takeuchi, K. Sorimachi, and T. Fujii: *Mater. Sci. Eng. A*, 1993, vol. 173, pp. 293–97.
43. Y. Miki and S. Takeuchi: *ISIJ Int.*, 2003, vol. 43, pp. 1548–55.
44. R. Singh, B.G. Thomas, and S.P. Vanka: *Metall. Mater. Trans. B*, 2014, vol. 45, pp. 1098–1115.
45. S.-M. Cho, S.-H. Kim, and B.G. Thomas: *ISIJ Int.*, 2014, vol. 54, pp. 855–64.
46. K. Jin, S.P. Vanka, and B.G. Thomas: *Metall. Mater. Trans. B*, 2016, vol. 37, pp. 1–17.
47. B. Thomas and R. Chaudhary: in *6th International conference on electromagnetic processing of materials (EPM)*, Electromagnetic Processing of Materials, Dresden, Germany, 2009, pp. 9–14.
48. H. Yu and M. Zhu: *ISIJ Int.*, 2008, vol. 48, pp. 584–91.
49. K. Jin, P. Kumar, S.P. Vanka, and B.G. Thomas: *Phys. Fluids 1994-Present*, 2016, vol. 28, p. 093301.
50. K. Jin, S.P. Vanka, and B. Thomas: in *Proc. 2nd Thermal and Fluid Eng. Conf, TFEC2017, 4th Int. Workshop on Heat Transfer*, ASTFE / Begell House Inc., Las Vegas, Nevada, USA, 2017, pp. 1–13.
51. R. Liu: Ph.D. Thesis, University of Illinois at Urbana-Champaign, 2015.
52. H. Kobayashi: *Phys. Fluids*, 2005, vol. 17, p. 045104.
53. H. Kobayashi: *Phys. Fluids*, 2008, vol. 20, p. 015102.
54. R. McDavid and B. Thomas: *Metall. Mater. Trans. B*, 1996, vol. 27, pp. 672–85.
55. F. Li, E. Wang, M. Feng, and Z. Li: *ISIJ Int.*, 2015, vol. 55, pp. 814–20.
56. P. Rossin and E. Rammler: *J Inst Fuel*, 1933, vol. 7, pp. 29–36.
57. H. Bai and B.G. Thomas: *Metall. Mater. Trans. B*, 2001, vol. 32, pp. 1143–59.
58. R. Liu, S.-M. Cho, B.G. Thomas, and S.-H. Kim: 2015.
59. J.T. Kuo and G.B. Wallis: *Int. J. Multiph. Flow*, 1988, vol. 14, pp. 547–64.
60. C.T. Crowe, J.D. Schwarzkopf, M. Sommerfeld, and Y. Tsuji: *Multiphase Flows with Droplets and Particles*, CRC Press, Boca Raton, 2011.
61. D. Legendre and J. Magnaudet: *J. Fluid Mech.*, 1998, vol. 368, pp. 81–126.
62. W.H. Press, S.A. Teukolsky, W.T. Vetterling, and B.P. Flannery: *Numerical Recipes in FORTRAN*, Cambridge University Press, Cambridge, 1992.
63. C.M. Winkler: Ph.D. Dissertation, Mechanical Engineering, University of Illinois, Urbana-Champaign, 2002.
64. A. Yoshizawa: *Phys. Fluids 1958-1988*, 1982, vol. 25, pp. 1532–38.
65. G. Marsaglia: *J. Stat. Softw.*, 2003, vol. 8, pp. 1–6.

66. S.P. Vanka: *J. Fluids Eng*., 2013, vol. 135, p. 061401.
67. A.F. Shinn: Ph.D. Thesis, University of Illinois at Urbana-Champaign, 2011.
68. R. Chaudhary: Ph.D. Thesis, University of Illinois at Urbana-Champaign, 2011.
69. P. Kumar, K. Jin, and S.P. Vanka: in *Proceedings of the 1st Thermal and Fluids Engineering Summer Conference*, American Society of Thermal and Fluids Engineers, New York City, 2016, pp. 1–17.
70. K. Jin, S.P. Vanka, and B.G. Thomas: *J. Fluids Eng*., 2015, vol. 137, p. 071104.
71. S.-M. Cho, B.G. Thomas, and S.-H. Kim: *Metall. Mater. Trans. B*, 2016, vol. 47, pp. 3080–98.
72. S. Yokoya, S. Takagi, S. Ootani, M. Iguchi, K. Marukawa, and S. Hara: *ISIJ Int*., 2001, vol. 41, pp. 1208–14.
73. S. Yokoya, S. Takagi, M. Iguchi, K. Marukawa, and S. Hara: *ISIJ Int*., 2001, vol. 41, pp. S47–51.
74. B.G. Thomas: *Iron Steel Technol*., 2006, vol. 3, p. 127.